DOI: 10.58895/ksp/1000162754-7 erschienen in:
Proceedings. 33. Workshop Computational Intelligence - Berlin, 23. – 24. November 2023
DOI: 10.5445/KSP/1000162754 | https://www.ksp.kit.edu/site/books/e/10.5445/KSP/1000162754/

Nonlinear Modeling and Control of 3-DOF Gyroscope Actuated Furuta Pendulum by Takagi-Sugeno Fuzzy Systems

Johannes Brunner[1], Nis Keilhauer[1], Vincent Vellguth[1], Heide Brandtstädter[1], Horst Schulte[1]

[1] HTW-Berlin University of Applied Sciences
E-Mail: brunner@htw-berlin.de, keilha@htw-berlin.de, vellguth@htw-berlin.de, h.brandtstaedter@htw-berlin.de, schulte@htw-berlin.de

Abstract

This paper presents the derivation of the equations of motion of a 3-DOF gyroscope with a pendulum attachment through the Euler-Lagrange approach, followed by a conversion into a Takagi-Sugeno Fuzzy Model. First, suitable coordinate frames and generalized coordinates are defined, followed by the definition of the kinetic energy of each body frame of the gyroscope. Next, the kinetic and potential energy of the pendulum attachment is described. The derived equations of motion are then validated by simulation and compared to the behavior of a testbed system (see Figure 1). The conversion to the Takagi-Sugeno fuzzy model is done by a weighted combination of locally valid linear models. A set of adequate premise variables and membership functions represent the nonlinear system. Finally, a controller synthesis through parallel distributed compensation and LMIs satisfying local quadratic Lyapunov functions is conducted and validated by simulation.

1 Introduction

The aim of this paper is to derive and validate the equations of motion of a "Control Moment Gyroscope" (CMG) with 3 degrees of freedom, extended by

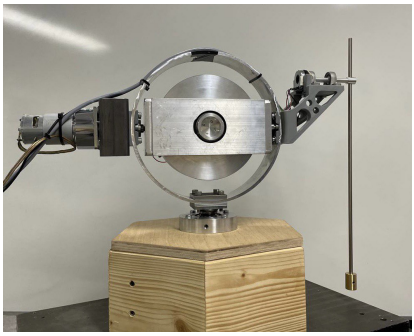

Figure 1: Testbed system

a pendulum attachement, similar to the testbed used in [1]. For the derivation, the modeling approaches of the CMG from [2] and the modeling approach of the Furuta pendulum in [3] are combined. The derived equations of motion are augmented with friction terms and validated using measurement data from the real testbed. Subsequently, the developed equations of motion are transformed into a Takagi-Sugeno formulation, and a Parallel Distributed Compensation (PDC) controller is derived using Linear Matrix Inequalitys (LMIs) to enforce closed-loop-dynamic constraints.

2 Methods

2.1 Nomenclature

The Notation in this Paper is as follows. Vectors are written italic with an underline $\underline{x}$, Matrices $\mathbf{A}$ bold and scalars s italic. Furthermore, $\prec$ and $\succ$ indicate negative and positive definiteness, respectively. $\mathbf{E}$ indicates the identity Matrix.

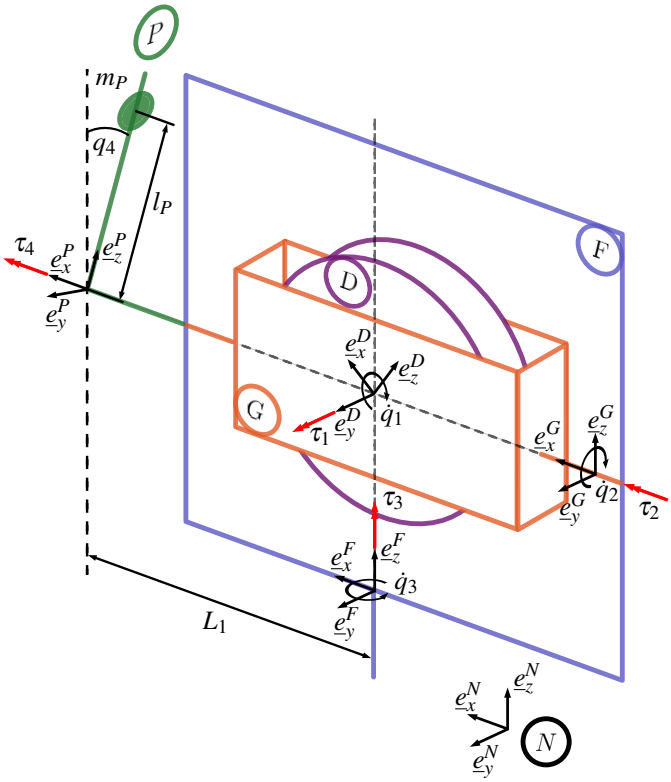

Figure 2: System sketch of the CMG Furuta Pendulum with 3 Degrees of freedom, the body frames, D, G, F, P and the reference frame N. For clarity the origins of the coordinate systems (except the Pendulum) are depicted with an offset.

2.2 Modelling

The CMG pendulum system in Figure 2 is described using five body frames, namely Disk (D), Gimbal (G), Frame (F), Pendulum (P), and the fixed reference frame (N). The coordinate systems are defined using the normal vectors $\underline{e}_i^j$ with $i = x, y, z$ as axes and $j = D, G, F, P, N$ as the associated body frame. The reference system N is chosen to be stationary, so that relative movements of the other reference systems in N constitute to an absolute velocity. The torques acting on the body frames are denoted as τ_n with $n = 1, 2, 3, 4$ along the corresponding rotational axis following the right hand rule.

The modelling of the CMG part of the overall system follow [2]. Therefore the generalized coordinates are chosen as:

$$\begin{aligned} \underline{q} &:= [q_1,\, q_2,\, q_3,\, q_4]^\top \\ \underline{\dot{q}} &:= [\dot{q}_1,\, \dot{q}_2,\, \dot{q}_3,\, \dot{q}_4]^\top \\ \underline{\ddot{q}} &:= [\ddot{q}_1,\, \ddot{q}_2,\, \ddot{q}_3,\, \ddot{q}_4]^\top, \end{aligned} \tag{1}$$

whereas q_1 represents the disk position about $\underline{e}_y^D$, q_2 represents the gimbal position about $\underline{e}_x^G$, q_3 represents the frame position about $\underline{e}_z^F$, and q_4 represents the pendulum position about $\underline{e}_x^P$. The controllable inputs of the system are the torques τ_1 and τ_2. Disturbance torques are τ_3 and τ_4. All torques are combined into the vector

$$\underline{\tau} := [\tau_1,\, \tau_2,\, \tau_3,\, \tau_4]^\top \tag{2}$$

The positive rotation directions of all coordinate systems follow the right-hand rule. Friction terms will be added at a later time. The center mass of the coordinate systems describing the CMG are assumed to be at the center of the disk. The mass center of the pendulum, denoted as m_P, has an effective pendulum length of l_P. The distance from the pendulum coordinate system's rotation axis to the frame's rotation axis is L_1. The moments of inertia of the bodies around different coordinate axes are represented in tensor form to calculate the kinetic energies for the Lagrange function.

$$\begin{aligned} \mathbf{I}_D^D &= \begin{bmatrix} J_{Dxx} & 0 & 0 \\ 0 & J_{Dyy} & 0 \\ 0 & 0 & J_{Dzz} \end{bmatrix}, \mathbf{I}_G^G = \begin{bmatrix} J_{Gxx} & 0 & 0 \\ 0 & J_{Gyy} & 0 \\ 0 & 0 & J_{Gzz} \end{bmatrix} \\ \mathbf{I}_F^F &= \begin{bmatrix} J_{Fxx} & 0 & 0 \\ 0 & J_{Fyy} & 0 \\ 0 & 0 & J_{Fzz} \end{bmatrix}, \mathbf{I}_P^P = \begin{bmatrix} J_{Pxx} & 0 & 0 \\ 0 & J_{Pyy} & 0 \\ 0 & 0 & J_{Pzz} \end{bmatrix} \end{aligned} \tag{3}$$

For the later description of the rotational positions of the bodies relative to each other rotation matrices are used. By combining the rotation matrices it is possible to represent all positions of the bodies in relation to the reference coordinate system. The rotation matrices $\mathbf{R}_i$ around the coordinate axes $i = x, y, z$ of the reference coordinate system are defined as follows:

$$\mathbf{R}_x(q_j) = \begin{bmatrix} 1 & 0 & 0 \\ 0 & \cos(q_j) & -\sin(q_j) \\ 0 & \sin(q_j) & \cos(q_j) \end{bmatrix}$$
$$\mathbf{R}_y(q_j) = \begin{bmatrix} \cos(q_j) & 0 & \sin(q_j) \\ 0 & 1 & 0 \\ -\sin(q_j) & 0 & \cos(q_j) \end{bmatrix} \tag{4}$$
$$\mathbf{R}_z(q_j) = \begin{bmatrix} \cos(q_j) & -\sin(q_j) & 0 \\ \sin(q_j) & \cos(q_j) & 0 \\ 0 & 0 & 1 \end{bmatrix}$$

Here, the notation $\mathbf{R}^i_j$ is introduced, which describes the rotation of the coordinate system j with respect to i.

$$\begin{aligned} \mathbf{R}^G_D &= \mathbf{R}_y(q_1) \\ \mathbf{R}^F_G &= \mathbf{R}_x(q_2) \\ \mathbf{R}^N_F &= \mathbf{R}_z(q_3) \\ \mathbf{R}^F_P &= \mathbf{R}_x(q_4) \end{aligned} \tag{5}$$

By multiplying the rotation matrices accordingly, it is possible to describe the rotation of any desired coordinate system of the CMG pendulum relative to the reference coordinate system.

$$\mathbf{R}^N_D = \mathbf{R}^N_F \mathbf{R}^F_G \mathbf{R}^G_D \tag{6}$$

With the rotation matrices, it is possible to represent the angular velocities of the different bodies in the reference coordinate system.

$$\underline{\omega}^N_{N,F} = [0^{3\times1}\ 0^{3\times1}\ \underline{Z}^N_N\ 0^{3\times1}]\underline{\dot{q}} \tag{7}$$

$$\underline{\omega}^N_{N,G} = [0^{3\times1}\ \underline{X}^N_F\ \underline{Z}^N_N\ 0^{3\times1}]\underline{\dot{q}} \tag{8}$$

$$\underline{\omega}^N_{N,D} = [\underline{Y}^N_G\ \underline{X}^N_F\ \underline{Z}^N_N\ 0^{3\times1}]\underline{\dot{q}} \tag{9}$$

with the rotational descriptions

$$\begin{aligned} \underline{Z}_N^N &= \underline{e}_z^N \\ \underline{X}_F^N &= \mathbf{R}_F^N \underline{e}_x^N \\ \underline{Y}_G^N &= \mathbf{R}_G^N \underline{e}_y^N \end{aligned} . \tag{10}$$

The matrices describing the rotations in (7), (8), and (9) are hereafter denoted as $\mathbf{J}_{N,k}^N$. Here examplary for the disk.

$$\mathbf{J}_{N,D}^N = [\underline{Y}_G^N \, \underline{X}_F^N \, \underline{Z}_N^N \, 0^{3\times 1}] \tag{11}$$

Additionally, the set of coordinate systems $\mathscr{S} = D, G, F$ is defined. From this, the kinetic energy $T_{\mathrm{CMG}}(\underline{q}, \underline{\dot{q}})$ of the CMG part of the overall system can be defined as:

$$T_{\mathrm{CMG}}(\underline{q}, \underline{\dot{q}}) = \frac{1}{2} \sum_{k \in \mathscr{S}} \underline{\dot{q}}^\top \left[\left(\mathbf{J}_{N,k}^N \right)^\top \mathbf{R}_k^N \mathbf{I}_k^k \left(\mathbf{R}_k^N \right)^\top \mathbf{J}_{N,k}^N \right] \underline{\dot{q}} \tag{12}$$

The description of the kinetic energy of the pendulum follow [3]. The linear velocity $\underline{v}_{\mathrm{P}}$ and angular velocity $\underline{\omega}_{\mathrm{P}}$ of the Pendulum are described separately and then combined. First the angular velocity of the pendulum arm is determined as follows:

$$\underline{\omega}_P = \mathbf{R}_P^F \cdot \begin{bmatrix} 0 \\ 0 \\ \dot{q}_3 \end{bmatrix} + \begin{bmatrix} \dot{q}_4 \\ 0 \\ 0 \end{bmatrix} = \begin{bmatrix} \dot{q}_4 \\ -\dot{q}_3 \sin(q_4) \\ \dot{q}_3 \cos(q_4) \end{bmatrix} \tag{13}$$

The linear velocity $\underline{v}_{\mathrm{P}}$ of the pendulum arm is composed of the translational velocity of the pendulum joint

$$\underline{v}_2 = \mathbf{R}_P^F \left(\underline{\omega}_{N,F}^N \times [L_1, \, 0, \, 0]^\top \right) = \begin{bmatrix} 0 \\ \cos(q_4) L_1 \dot{q}_3 \\ \sin(q_4) L_1 \dot{q}_3 \end{bmatrix} \tag{14}$$

and the translational velocity of the pendulum center mass

$$\underline{v}_{b,m} = \underline{\omega}_P \times [\,0,\,0,\,l_P]^\top = \begin{bmatrix} -\sin(q_4) l_P \dot{q}_3 \\ -l_P \dot{q}_4 \\ 0 \end{bmatrix} \tag{15}$$

which results in

$$\underline{v}_P = \underline{v}_2 + \underline{v}_{b,m} = \begin{bmatrix} -\sin(q_4) l_P \dot{q}_3 \\ \cos(q_4) L_1 \dot{q}_3 - l_P \dot{q}_4 \\ \sin(q_4) L_1 \dot{q}_3 \end{bmatrix}. \tag{16}$$

The kinetic energy of the pendulum is then given by

$$T_P(\underline{q}, \dot{\underline{q}}) = \frac{1}{2} \left(\underline{v}_P^\top (m_P \mathbf{E}^{3\times 3}) \underline{v}_P + (\underline{\omega}_P)^\top \mathbf{I}_P^p \underline{\omega}_P \right), \tag{17}$$

where $\mathbf{E}$ represents the identity matrix. Since the pendulum has potential energy, and the reference height is chosen at $q_4 = \pi$ (hanging pendulum), the potential energy of the Pendulum V_P is

$$V_P(\underline{q}) = g \cdot m_P \cdot l_P (1 + \cos(q_4)) \tag{18}$$

With the kinetic and potential energy of all bodies, the Lagrangian can be formulated as

$$\mathscr{L}(\underline{q}, \dot{\underline{q}}) = T_{CMG}(\underline{q}, \dot{\underline{q}}) + T_P(\underline{q}, \dot{\underline{q}}) - V_P(\underline{q}). \tag{19}$$

Now, the equations of motion can be derived using the Euler-Lagrange formalism:

$$\frac{d}{dt} \left(\frac{\partial \mathscr{L}(\underline{q}, \dot{\underline{q}})}{\partial \dot{\underline{q}}} \right) - \frac{\partial \mathscr{L}(\underline{q}, \dot{\underline{q}})}{\partial \underline{q}} = \underline{\tau} \tag{20}$$

Due to the total number of bodies, four moving equations are derived describing the acceleration of the different bodies.

For the formulation of the Lagrangian from (19), the Symbolic Toolbox in MATLAB is used, and the Euler-Lagrange equations were derived according to (20) using the community function "EulerLagrange".

2.3 Takagi-Sugeno System

The TS-Model is constructed via local linearization; therefore, consider the nonlinear system

$$\begin{aligned} \dot{\underline{x}} &= \underline{f}(\underline{x}, \underline{u}) \\ \underline{y} &= \underline{h}(\underline{x}) \end{aligned} \tag{21}$$

Through the first-order Taylor Series Expansion, we obtain the matrices

$$\mathbf{A}_i = \left.\frac{\partial \underline{f}}{\partial \underline{x}}\right|_c \qquad \mathbf{B}_i = \left.\frac{\partial \underline{f}}{\partial \underline{u}}\right|_c \qquad \mathbf{C}_i = \left.\frac{\partial \underline{h}}{\partial \underline{x}}\right|_c, \tag{22}$$

where c describes the linearization point. We then formulate the TS-System, where all linear submodels are blended into each other by the membership functions $h_i(\underline{z})$

$$\begin{aligned} \dot{\underline{x}} &= \sum_{i=1}^{N_r} h_i(\underline{z}) \left(\mathbf{A}_i \underline{x} + \mathbf{B}_i \underline{u} + \underline{a}_i\right) \\ \underline{y} &= \sum_{i=1}^{N_r} h_i(\underline{z}) \mathbf{C}_i \underline{x} + \underline{c}_i \end{aligned} \tag{23}$$

where $\underline{z}$ denotes the vector of premise variables that determine which model is active at any given time, N_r is the number of linearization points [4]. The membership functions $h_i(\underline{z})$ are chosen to be triangular and fulfill the properties $1 \geq h_i(\underline{z}) \geq 0$ and $\sum_{i=1}^{N_r} h_i(\underline{z}) = 1$. Each submodel i represents the nonlinear system at the linearization point c to 100%, i.e., if $h_1 = 1$, only the submodel $\dot{\underline{x}} = \mathbf{A}_1 \underline{x} + \mathbf{B}_1 \underline{u} + \underline{a}_1$ would be active and represent the current dynamics fully [5]. The affine terms $\underline{a}_i$ and $\underline{c}_i$ of non-equilibrium linearization points are computed as follows:

$$\begin{aligned} \underline{a}_i &= \underline{f}(\underline{x}_c, \underline{u}_c) - \mathbf{A}_i \underline{x}_c - \mathbf{B}_i \underline{u}_c \\ \underline{c}_i &= \underline{h}(\underline{x}_c) - \mathbf{C}_i \underline{x}_c \end{aligned} \tag{24}$$

It is noted here that, for simplicity reasons, the affine terms are neglected for controller synthesis.

2.4 Parallel Distributed Compensation

The fuzzy controller formulation is done in a similar manner as the TS-Model by utilizing local controller gains for each linearization point c and blending these together with the membership functions $h_i(\underline{z})$ of the model as the premise variables $\underline{z}$ change [6].

$$\underline{u} = -\sum_{i=1}^{N_r} h_i(\underline{z}) \mathbf{K}_i \underline{x} \tag{25}$$

Augmenting (25) into (23) and neglecting the affine term $\underline{a}_i$ yields the closed-loop TS-System of the form:

$$\dot{\underline{x}} = \sum_{i=1}^{N_r} \sum_{j=1}^{N_r} h_i(\underline{z}) h_j(\underline{z}) \{\mathbf{A}_i - \mathbf{B}_i \mathbf{K}_j\} \underline{x} \tag{26}$$

Which can be written in compact form:

$$\dot{\underline{x}} = \sum_{i=1}^{N_r} \sum_{j=1}^{N_r} h_i(\underline{z}) h_j(\underline{z}) \mathbf{G}_{ij} \underline{x} \tag{27}$$

2.5 Controller Synthesis via LMIs

For controller synthesis, the local quadratic Lyapunov functions are applied:

$$V_i(\underline{x}) = \underline{x}^\top \mathbf{P}_i \underline{x} \tag{28}$$

$$\dot{V}_i(\underline{x}) = \dot{\underline{x}}^\top \mathbf{P}_i \underline{x} + \underline{x}^\top \mathbf{P}_i \dot{\underline{x}} \tag{29}$$

where $\mathbf{P}_i$ is a symmetric, positive definite matrix. To find controller gains, we augment (29) with (27) and define $\mathbf{P}_i = \mathbf{X}_i^{-1}$ and $\mathbf{K}_j = \mathbf{M}_i \mathbf{X}_i^{-1}$ as for each local controller j the LMIs are solved independently thus $i = j$ for controller

synthesis. The requirements for asymptotic lyapunov stability:

$$\begin{aligned} V_i(\underline{x}) &> 0, \ \ \forall \underline{x} \neq 0 \\ V_i(\underline{x}) &= 0, \ \ \underline{x} = 0 \end{aligned} \tag{30}$$

$$\dot{V}_i(\underline{x}) < 0, \ \ \forall \underline{x} \neq 0 \tag{31}$$

can then be expressed in LMIs which constrain convex sets in the complex plane [7]. The so-called $\mathscr{D}$-Region LMI constraint then results in the formulation:

Find a matrix $\mathbf{X}_i = \mathbf{X}_i^\top \succ 0$ and $\mathbf{M}_i$ for a desired $\alpha \geq 0$, $r > \alpha$, and $\theta > 0$ under the constraint:

$$\mathbf{X}_i\mathbf{A}_i^\top + \mathbf{A}_i\mathbf{X}_i - \mathbf{M}_i^\top\mathbf{B}_i^\top - \mathbf{B}_i\mathbf{M}_i + 2\alpha\mathbf{X}_i \prec 0, \tag{32}$$

$$\begin{bmatrix} -r\mathbf{X}_i & \mathbf{A}_i\mathbf{X}_i - \mathbf{B}_i\mathbf{M}_i \\ \mathbf{X}_i\mathbf{A}_i^\top - \mathbf{M}_i^\top\mathbf{B}_i^\top & -r\mathbf{X}_i \end{bmatrix} \prec 0, \tag{33}$$

$$\begin{bmatrix} \sin\theta(\mathbf{X}_i\mathbf{A}_i^\top + \mathbf{A}_i\mathbf{X}_i - \mathbf{M}_i^\top\mathbf{B}_i^\top - \mathbf{B}_i\mathbf{M}_i) \\ \cos\theta(\mathbf{X}_i\mathbf{A}_i^\top - \mathbf{M}_i^\top\mathbf{B}_i^\top - \mathbf{A}_i\mathbf{X}_i + \mathbf{B}_i\mathbf{M}_i) \\ \qquad\qquad \cos\theta(\mathbf{A}_i\mathbf{X}_i - \mathbf{B}_i\mathbf{M}_i - \mathbf{X}_i\mathbf{A}_i^\top + \mathbf{M}_i^\top\mathbf{B}_i^\top) \\ \qquad\qquad \sin\theta(\mathbf{A}_i\mathbf{X}_i - \mathbf{B}_i\mathbf{M}_i + \mathbf{X}_i\mathbf{A}_i^\top - \mathbf{M}_i^\top\mathbf{B}_i^\top) \end{bmatrix} \prec 0 \tag{34}$$

where α denotes the minimum required decay rate, r defines the radius of a half circle toward the complex left-hand open plane with the origin in the center of the complex plane, and θ defines the angle between the real axis and a cone restriction toward the complex open left-hand plane [8].

As the $\mathscr{D}$-Region constraint might not be ideal for the coupled dynamics of the system (all states underlie the same decay constraints α), an optimal controller design is pursued as well. The optimal controller LMI approach from [6] is used, utilizing the performance function:

$$J = \int_0^\infty \{\underline{y}^\top(t)\mathbf{W}\underline{y}(t) + \underline{u}^\top(t)\mathbf{R}\underline{u}(t)\}dt \tag{35}$$

The cost function (35) results in the minimization problem $J < \underline{x}^\top(0)\mathbf{P}_i\underline{x}(0) < \lambda$ with the following LMI constraints:

$$\min_{\mathbf{X}_i,\mathbf{M}_i,\mathbf{Y}_{0,i}} \lambda$$

subject to

$$\mathbf{X}_i \succ 0, \qquad \mathbf{Y}_{0,i} \succeq 0, \tag{36}$$

$$\begin{bmatrix} \lambda & \underline{x}^\top(0) \\ \underline{x}(0) & \mathbf{X}_i \end{bmatrix} \succ 0, \tag{37}$$

$$\hat{\mathbf{U}}_{ii} + (s-1)\mathbf{Y}_{3,i} \prec 0, \tag{38}$$

where $s > 1$

$$\hat{\mathbf{U}}_{ii} = \begin{bmatrix} \begin{pmatrix} \mathbf{X}_i\mathbf{A}_i^\top + \mathbf{A}_i\mathbf{X}_i \\ -\mathbf{B}_i\mathbf{M}_i - \mathbf{M}_i^\top\mathbf{B}_i^\top \end{pmatrix} & \mathbf{X}_i\mathbf{C}_i^\top & -\mathbf{M}_i^\top \\ \mathbf{C}_i\mathbf{X}_i & -\mathbf{W}^{-1} & \mathbf{0} \\ -\mathbf{M}_i & \mathbf{0} & -\mathbf{R}^{-1} \end{bmatrix} \tag{39}$$

$$\mathbf{Y}_{3,i} = \text{block-diag}(\mathbf{Y}_{0,i}, \mathbf{0}, \mathbf{0})$$

The optimization problem above is in a reduced form from [6], as stability is only demanded for the local models and no combination of $i \neq j$ as well as the relaxed stability condition where s is the maximum number of submodels that are active at the same time. The weighting matrices $\mathbf{W}$ and $\mathbf{R}$ are chosen constant and do not deviate for different local constraints.

For handling the LMIs, the YALMIP interface together with the solver MOSEK is used [9],[10].

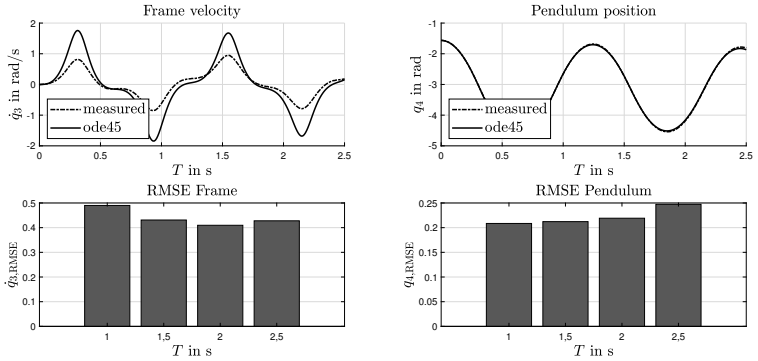

Figure 3: State comparison between the nonlinear CMG Furuta Pendulum equations evaluated using MATLAB's ode45 solver and measurements of the testbed system on the top, and RMSE errors at the bottom with $\dot{q}_1 = 0$ rad/s.

3 Results

3.1 Model Validation

The derived nonlinear equations of motion for the CMG Furuta Pendulum from the Euler-Lagrange approach (20) are simulated using the parameters provided in Table 1. The simulations are carried out using the MATLAB ode45 solver and are compared to measured values obtained from the testbed system. The comparison is evaluated through the Root Mean Squared Error (RMSE):

$$\mathrm{RMSE} = \sqrt{\frac{1}{N}\sum_{k=1}^{N}(y(k)-\hat{y}(k))^2} \tag{40}$$

for time intervals of 1, 1.5, 2, and 2.5 seconds. Two different sets of measurements are taken while the pendulum is falling from its upright position. For the first measurement, the disk is not spinning ($\dot{q}_1 = 0$ rad/s), and the states $\underline{x}_{\mathrm{meas},1} = [\dot{q}_3, q_4]^\top$ are measured, as depicted in Figure 3. At this point, the system essentially represents a Furuta Pendulum with the center of mass of the cantilever arm at the center of rotation of the frame.

Table 1: Systen Parameters of the CMG Furuta Pendulum testbed system

Variable	Value	Unit
J_{Dxx}	0.0027	kg m^2
J_{Dyy}	0.0048	kg m^2
J_{Dzz}	0.0027	kg m^2
J_{Gxx}	0.0014	kg m^2
J_{Gyy}	0.005	kg m^2
J_{Gzz}	0.005	kg m^2
J_{Fxx}	0	kg m^2
J_{Fyy}	0	kg m^2
J_{Fzz}	0.0414	kg m^2
J_{Pxx}	0.003	kg m^2
J_{Pyy}	0.003	kg m^2
J_{Pzz}	0	kg m^2
μ_1	0.8	kg m s^{-1}
μ_2	7.2	kg m s^{-1}
μ_3	0.7	kg m s^{-1}
μ_4	0.135	kg m s^{-1}
L_1	0.254	m
l_P	0.246	m
m_P	0.216	kg

The second measurement is taken with the disk spinning at its maximum speed, $\dot{q}_{1,\max} = 28.8$ rad/s. In this case, the states $\underline{x}_{\text{meas},2} = [q_2, \dot{q}_3, q_4]^\top$ are measured to observe the effect of precession on the gimbal states and vice versa, as shown in Figure 4.

In the first measurement, the pendulum angle q_4 shows an RMSE of around 0.2 up to 2 seconds, whereas the frame angular velocity $\dot{q}_3$ exhibits an RMSE of around 0.4. The frame velocity measurements particularly deviate from the simulation at the peaks, where the frame is accelerated due to the falling pendulum. The second measurement shows that the measured and simulated states strongly differ from each other. It is presumed that this discrepancy is due to the neglect of the motor actuating the disk, which is attached along the y-axis of the gimbal coordinate frame. The motor has a gearbox, increasing its weight and potentially offsetting the center of mass of the gimbal. Therefore,

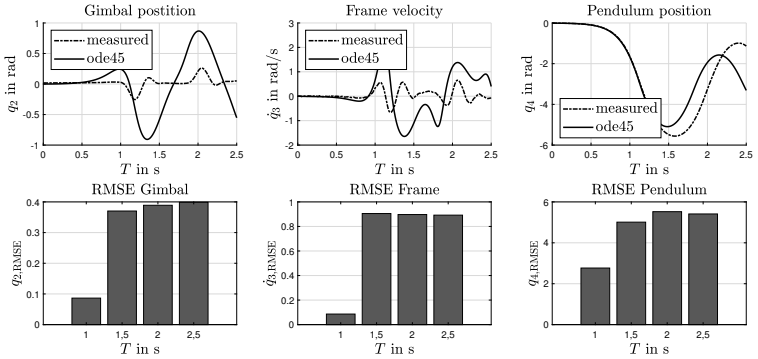

Figure 4: State comparison between the nonlinear CMG Furuta Pendulum equations evaluated using MATLAB's ode45 solver and measurements of the testbed system on the top, and RMSE errors at the bottom with $\dot{q}_1 = 28.8$ rad/s.

the assumption that all CMG center masses are located in the center of the CMG is not valid for the measured values.

Table 1 displays the system parameters for the testbed system, which were obtained through the CAD program Inventor, using an internal Finite Element Method (FEM) to calculate the inertia of the components.

3.2 Controller Design

The state feedback control structure is depicted in Figure 5. The controllable inputs of the system are $u_1 = \tau_1$ and $u_2 = \tau_2$. The torque τ_1 actuating the disk is not controlled and is kept at a constant value to ensure the disk spins at its highest angular velocity. Input u_2 is controlled via the PDC control law with controller parameters synthesized through the LMI formulations given in Section: Controller Synthesis. As premise variables, the current gimbal and pendulum angles $\underline{z} = [q_2, q_4]^\top$ are used. The disk position and velocity are neglected for the state feedback controller, leaving the states $\underline{x}_{\mathrm{cntrl}} = [q_2, \dot{q}_2, q_3, \dot{q}_3, q_4, \dot{q}_4]^\top$ to be controlled via the PDC.

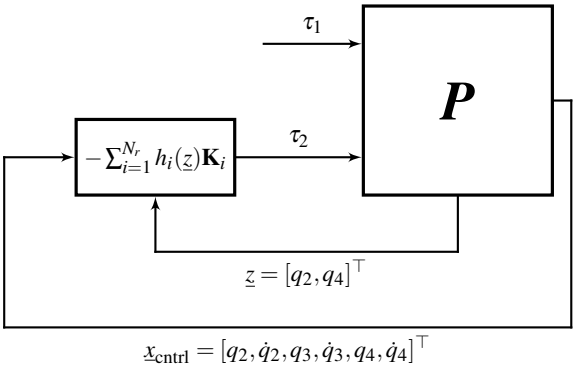

Figure 5: Basic Control Structure, $\boldsymbol{P}$ resembles the Plant, $\underline{z}$ the premise vector, τ_1 and τ_2 the inputs u_1 and u_2 into the system respectively and $\underline{x}_{\text{cntrl}}$ the controlled system states

The linearization points are chosen as $q_2 \in [-1.2,\ 1.2]$ rad for the gimbal angle and $q_4 \in [-0.5236,\ 0.5236]$ rad for the pendulum angle. The disk speed is set to $\dot{q}_1 = 28.8$ rad/s for Scenario 1 (Low-Speed Disk) and $\dot{q}_1 = 45$ rad/s for Scenario 2 (High-Speed Disk).

Scenario 1 yields the following submodels of the TS-System:

$$\mathbf{A}_{1,4,\text{cntrl}} = \begin{bmatrix} 0 & 1 & 0 & 0 & 0 & 0 \\ 0 & -7.2 & 0 & 12.41 & 0 & 0 \\ 0 & 0 & 0 & 1 & 0 & 0 \\ 0.115 & -0.89 & 0 & -0.7 & 2.47 & 0 \\ 0 & 0 & 0 & 0 & 0 & 1 \\ 0.081 & -0.65 & 0 & 0 & 28.41 & -0.14 \end{bmatrix} \tag{41}$$

$$\mathbf{A}_{2,3,\text{cntrl}} = \begin{bmatrix} 0 & 1 & 0 & 0 & 0 & 0 \\ 0 & -7.2 & 0 & 12.41 & 0 & 0 \\ 0 & 0 & 0 & 1 & 0 & 0 \\ -0.115 & -0.89 & 0 & -0.7 & 2.47 & 0 \\ 0 & 0 & 0 & 0 & 0 & 1 \\ -0.081 & -0.65 & 0 & 0 & 28.41 & -0.14 \end{bmatrix} \tag{42}$$

Table 2: $\mathscr{D}$-Region constraints and Optimal Controller weighting for Low-Speed Disk (Scenario 1) and High-Speed Disk (Scenario 2) controller synthesis.

Scenario	$\mathscr{D}$-Region	Optimal Controller
1	$\theta = 0.5236$ rad $\alpha = 2$ $r = 10$	$\mathbf{W} = \mathrm{diag}(0.1, 0.001, 0.1, 0.0001, 1, 0.001)$ $\mathbf{R} = 0.3$ $\lambda = 0.2$ $\underline{x}(0) = [0,0,0,0,0.27,0]^\top$
2	$\theta = 0.5236$ rad $\alpha = 2$ $r = 10$	$\mathbf{W} = \mathrm{diag}(0.1, 0.001, 0.1, 0.0001, 1, 0.001)$ $\mathbf{R} = 0.3$ $\lambda = 0.1$ $\underline{x}(0) = [0,0,0,0,0.37,0]^\top$

$$\mathbf{B}_{1,3,\mathrm{cntrl}} = \begin{bmatrix} 0 & 0 \\ 0 & 264.61 \\ 0 & 0 \\ 16.6 & 0 \\ 0 & 0 \\ 12.1 & 0 \end{bmatrix}, \quad \mathbf{B}_{2,4,\mathrm{cntrl}} = \begin{bmatrix} 0 & 0 \\ 0 & 264.61 \\ 0 & 0 \\ -16.6 & 0 \\ 0 & 0 \\ -12.1 & 0 \end{bmatrix} \tag{43}$$

The parameters for controller synthesis in the different scenarios are listed in Table 2. The input $u_2 = \tau_2$ is limited to 2.5 Nm, which is the maximum torque of the actuating motor for the gimbal.

For scenario 1 we obtain the different gain sets for the $\mathscr{D}$-Region controller

$$\begin{aligned} \mathbf{K}_{1,4,\mathscr{D}} &= [-7.44, 0.075, -6.01, -8.15, -14.47, -1.99] \\ \mathbf{K}_{2,3,\mathscr{D}} &= [7.66, 0.076, 6.41, 9.8, -14.32, -3.49] \end{aligned} \tag{44}$$

and the optimal controller:

$$\begin{aligned} \mathbf{K}_{1,4,\mathrm{opt}} &= [-0.098, 0.13, -0.004, 0.102, -15.48, -2.87] \\ \mathbf{K}_{2,3,\mathrm{opt}} &= [-0.087, 0.15, 0.051, 0.17, -17.48, -3.32] \end{aligned} \tag{45}$$

Table 3: Initial conditions for Low Speed Disk (Scenario 1) and High Speed Disk (Scenario 2) simulation studies.

Scenario	$\mathscr{D}$-Region	Optimal Controller
1	$x_0 = [0, 28.8, 0, 0, 0, 0, 0.2, 0]^\top$	$x_0 = [0, 28.8, 0, 0, 0, 0, 0.27, 0]^\top$
2	$x_0 = [0, 45, 0, 0, 0, 0, 0.2, 0]^\top$	$x_0 = [0, 45, 0, 0, 0, 0, 0.37, 0]^\top$

3.3 Simulation Studies

In total four simulation studies are conducted to find the maximum initial angle q_4 of the pendulum the controller is able to return into the unstable equilibrium $q_4 = 0$ rad.

1. Disk spinning at $\dot{q}_1 = 28.8$ rad/s, $\mathscr{D}$-Region constraints
2. Disk spinning at $\dot{q}_1 = 28.8$ rad/s, Optimal controller design
3. Disk spinning at $\dot{q}_1 = 45$ rad/s, $\mathscr{D}$-Region constraints
4. Disk spinning at $\dot{q}_1 = 45$ rad/s, Optimal controller design

The simulation setups allow for comparison between the two different controller synthesis procedures. The increase in angular velocity of the Disk from $\dot{q}_1 = 28.8$ to $\dot{q}_1 = 45$ rad/s shows if control performance can be improved by increasing the dynamic of the actuator. As the actuating torque moving the Frame through precession is defined as

$$\tau_3 = \dot{q}_2 \cdot \dot{q}_1 \cdot J_{Dyy} \cdot \cos(q_2) \tag{46}$$

As the goal of the Simulations is to find the maximum angle q_4 the controller is able to recover the initial conditions for the different scenarios are listed in Table 3. The results show, that the maximum initial angle for the $\mathscr{D}$-Region controller is $q_4 = 0.2$ rad for Scenario 1 and Scenario 2. The optimal controller was able to recover the Pendulum from $q_4 = 0.27$ for Scenario 1 and $q_4 = 0.37$ rad for Scenario 2.

The simulation results are depicted in Figures 6, 7, and 8. Two main findings can be obtained. Firstly the simulations indicate a limited stability region

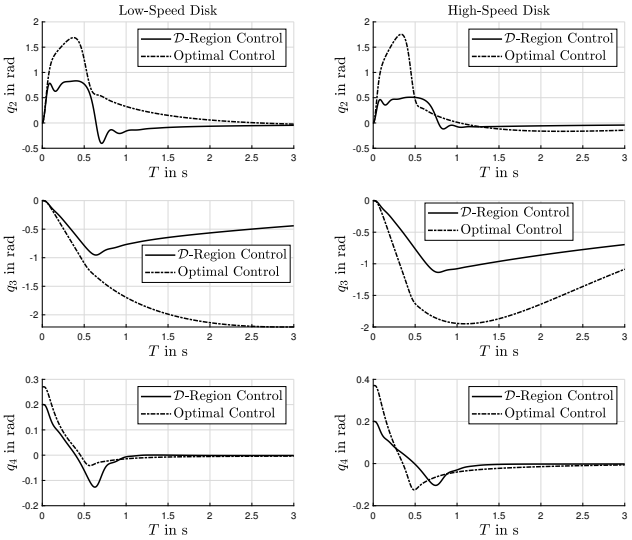

Figure 6: Gimbal, Frame, and Pendulum angles q_2, q_3 and q_4 respectively for Low-Speed Disk and High-Speed Disk scenarios as well as a comparison between $\mathscr{D}$-Region and Optimal Controller

independent of controller synthesis due to various factors. The torque τ_3 is limited by the velocity of the disk $\dot{q}_1$, and the maximum torque τ_2 enforced by the motor moving the gimbal limits $\dot{q}_2$ as seen in (46). Most notable is the $\cos(q_2)$ term from the precession in (46) if the gimbal is moved towards the angle $q_2 \to \pm\pi/2$ the effect on the frame through actuating the gimbal decreases significantly.

Secondly, the simulations indicate that the decay constraints imposed by the $\mathscr{D}$-Region have a negative impact on the maximum recoverable initial pendulum angle q_4. This is likely induced by the coupled dynamics of the system, as the body acting on the pendulum is the frame, which is actuated by the gimbal movement.

Increasing the Disk angular velocity to 45 rad/s for Scenario 2 also increases the angular momentum of the disk proportionally, therefore increasing τ_3 by actuating the Gimbal with τ_2.

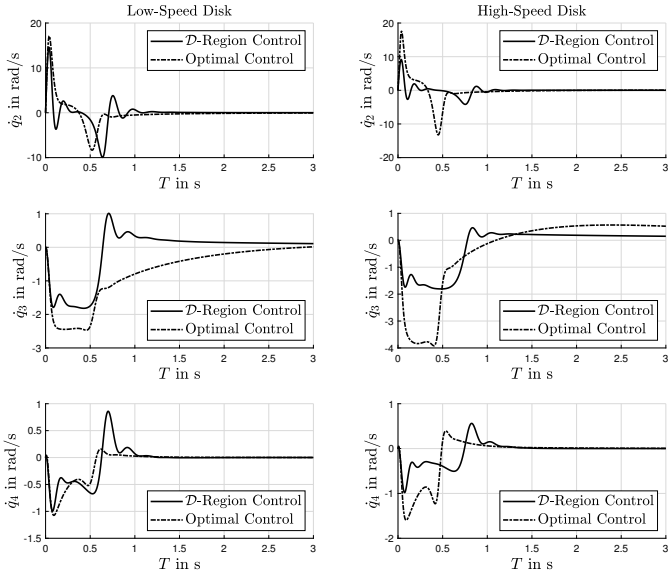

Figure 7: Gimbal, Frame and Pendulum angular velocities $\dot{q}_2$, $\dot{q}_3$ and $\dot{q}_4$ respectively for Low-Speed Disk and High-Speed Disk scenarios as well as a comparison between $\mathscr{D}$-Region and Optimal controller

Figure 8 displays the torque τ_2 demanded by the controller, which acts on the gimbal. It can be observed that at the beginning of the simulation, the recovery of the pendulum angle q_4 has the most significant impact on the demanded torque. The $\mathscr{D}$-Region controller and the optimal controller exhibit different behaviors when the pendulum angle is recovered and stabilized. This difference is due to the less conservative decay constraints for the optimal controller on the states, excluding the pendulum position, which is also evident in Figures 6 and 7.

4 Discussion

The results presented in this paper demonstrate the capability of a Takagi-Sugeno Parallel Distributed Compensation (PDC) fuzzy controller to stabilize a highly nonlinear Control Moment Gyroscope (CMG)-actuated Furuta

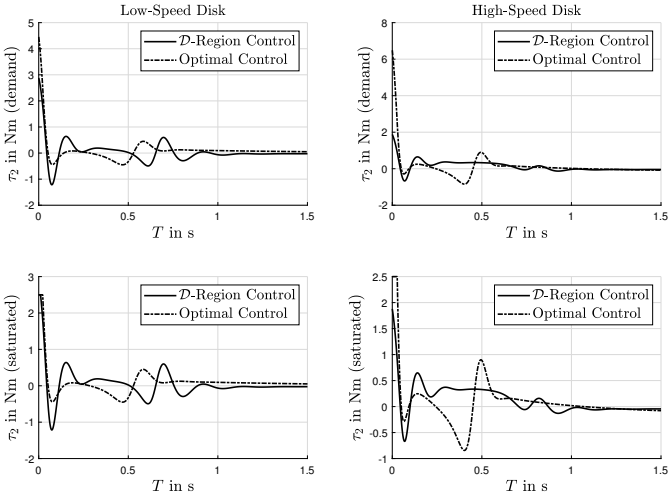

Figure 8: Demanded and saturated input torque $u_2 = \tau_2$ for Low Speed Disk and High Speed Disk scenarios as well as comparison between $\mathcal{D}$-Region and Optimal controller

Pendulum at an unstable equilibrium point. It is found that the dynamics of the torque generated through precession, in combination with the controller design, have an impact on the maximum initial pendulum angle the controller is able to recover to its unstable equilibrium. In an optimal controller design, where the closed-loop dynamics of each state can be weighted independently, the controller can exceed a common decay rate constraint through LMIs, especially when the actuator dynamics are high, and the system dynamics are strongly coupled, as in the testbed system. Shortcomings primarily lie in the identification of the system behavior when the disk is spinning. Therefore, an adjustment in the hardware and weight distribution of the gimbal might yield better results. Furthermore, the current testbed system has cables running off the motor that actuates the gimbal, as seen in Figure 1, introducing random friction terms due to the current cable positions. An adaptation to slip rings might be advantageous, eliminating random friction terms.

Furthermore, the current linearization points are chosen to include a wide range of angles the pendulum and gimbal can have during the recovery of the pen-

dulum angle. Performance might be improved by increasing the number of linearization points.

It is noted, that the $\mathscr{D}$-Region constraints were not further optimized after showing acceptable performance therefore the $\mathscr{D}$-Region controller might show some room for improvement.

The angles the controllers are able to recover are quite small indicating a limitation of the dynamics of the system under current actuating forces. Therfore the current Hardware is subject to improvement to increase overall dynamics of the system.

5 Conclusion

The control of a testbed system similar to the one investigated in this paper is, to the knowledge of the authors, only conducted in [1] where an LPV approach is pursued. [1] does focus on the swing up of the system and does not include an investigation of the stabilizing controller for the unstable equilibrium. It is only stated, that the switching between the swing-up controller and stabilizing controller is executed at a Pendulum angle $|q_x| < 0.15$ rad and the LPV scheduling region ranges from $q_2 \in [-60^\circ,\ 60^\circ]$ and $\omega_1 = \dot{q}_1 \in [30\ \text{rad/s},\ 60\ \text{rad/s}]$. This paper presents an alternative control concept for the stabilizing controller through a Fuzzy TS approach and LMIs which in Scenario 2 achieved a stable recovery of the Pendulum from an initial angle of $q_4 = 0.37$ rad under ideal conditions and Single Input only actuating the Gimbal through the controller.

As the system parameters in [1] differ from the one in this work it is to be investigated, if the Fuzzy controller is able to show similar performance when adapting the system parameters to match the system in [1].

It is mentioned here, that for the system parameters [1] refers to [11] where the inertia Tensores might not be correctly given in comparison to the system sketch. [12] is dated later than [11] where the inertia Tensors are corrected. [11] and [12] refer to the manual of the testbed system ECP 750 (Educational Control Products) which is to the knowledge of the authors not accessible publicly.

6 Future Work

Future work could include an extension to a multi-input system where the torque τ_2 is actuated through the controller as well as conducted in [1]. The premise variables could be extended to incuding the current Disk velocity $\dot{q}_1$. Also the $\mathscr{D}$-Region and optimal controller constraints can be altered for each linearization point increasing flexibility for controller design. As the number of linearization points is quite small, the controller synthesis could also be extended to find a global lyapunov function.

Another object of future work is the design of a Fuzzy TS swing-up controller, where further linearization points as well as an extension of the premise vector might yield satisfying results.

A significant improvement of the testbed system is the adaptation of the Hardware, real life tests can then be performed to show the performance of the controller on the Hardware itself. The controller synthesis therefore can be extended to an optimal-robust approach to ensure robustness against model uncertainty.

References

[1] Patrick J. W. Koelewijn, Pablo S. G. Cisneros, Herbert Werner, Roland Toth. “LPV Control of a Gyroscope with Inverted Pendulum Attachment”. In: *2nd IFAC Workshop on Linear Parameter Varying Systems LPVS 2018*. vol. 51, no. 26, pp. 49-54, 2018. IFAC-PapersOnLine.

[2] Tom Bloemers, Roland Toth. “Equations of Motion of a Control Moment Gyroscope”, 2019.

[3] Benjamin Seth Cazzolato, Zebb Prime. “On the Dynamics of the Furuta Pendulum”. In: *Journal of Control Science and Engineering*, 2011.

[4] Zsofia Lendek, Thierry Marie Guerra, Robert Babuska, Bart De Schutter, “Stability Analysis and Nonlinear Observer Design Using Tagaki-Sugeno Fuzzy Models”, 2011.

[5] M. Johansson, A. Rantzer, K.-E. Arzen, “Piecewise Quadratic Stability of Fuzzy Systems”, In: *IEEE Transactions on Fuzzy Systems*, vol. 7, no. 6, pp. 713-722, 1999.

[6] Kazuo Tanaka, Hua Wang. “Fuzzy Control Systems Design and Analysis: A Linear Matrix Inequality Approach”. 2001.

[7] Carsten Scherer, Siep Weiland. “Linear Matrix Inequalities in Control”. Lecture Notes. 2015.

[8] Florian Pöschke, Eckhard Gauterin, Horst Schulte, “Chapter 2 - LMI Region-Based Nonlinear Disturbance Observer With Application to Robust Wind Turbine Control”, In: *New Trends in Observer-based Control*, Academic Press, pp. 35-75, year 2019, Series: Emerging Methodologies and Applications in Modelling.

[9] J. Lofberg, “YALMIP: A Toolbox for Modeling and Optimization in MATLAB”, In: *2004 IEEE International Conference on Robotics and Automation (IEEE Cat. No.04CH37508)*, year 2004, pp. 284-289.

[10] MOSEK ApS, “The MOSEK Optimization Toolbox for MATLAB Manual. Version 10.0.”, year 2023, URL: `http://docs.mosek.com/10.0/toolbox/index.html`.

[11] Hossam S. Abbas, Ahsan Ali, Seyed M. Hashemi, Herbert Werner. “LPV Gain-Scheduled Control of a Control Moment Gyroscope”. In: *2013 American Control Conference*, Washington, DC, USA, 2013, pp. 6841-6846.

[12] Hossam Abbas, Ahsan Ali, Seyed Hashemi, Herbert Werner, “LPV State-Feedback Control of a Control Moment Gyroscope”, In: *Control Engineering Practice*, vol. 24, pp. 129-137, year 2014.